buildings

MDPI

Article

Downburst-Induced Vibration Coefficient of Long-Span Roof Structures

Chaohao Chen , Linsheng Huo *, Ziru Wang and Hongnan Li

State Key Laboratory of Coastal and Offshore Engineering, Dalian University of Technology, Dalian 116024, China; 17chchen@mail.dlut.edu.cn (C.C.); wangziru26@126.com (Z.W.); hnli@dlut.edu.cn (H.L.)
* Correspondence: lshuo@dlut.edu.cn

Abstract: Long-span roof structures are vulnerable to being damaged by downbursts due to the sensitivity of such structures to wind loads. However, there is still no simple and practical method for the downburst-resistant design of such structures to date. Inspired by the wind-induced vibration coefficient (WVC) frequently used by engineers, this paper proposes a downburst-induced vibration coefficient (DVC) to evaluate the response of a roof structure subjected to downbursts. The proposed DVC is defined as the ratio of the total response to the mean response of the structure due to the action of downburst wind loads. The influences of different parameters on the downburst-induced vibration response of a long-span single-layer spherical reticulated structure are first analyzed in detail. Then, using a statistical approach, a design DVC, which can be practically adopted for civil engineers to evaluate the total structural response, is proposed to facilitate the structural downburst-resistant design. With the influences of different structural parameters fully taken into consideration, the design DVCs of displacement and internal force are studied through orthogonal analysis. Finally, regression models of the design DVCs are presented, and their reliability is verified via the application to a case study. The verification results indicate that the proposed regression models of the design DVCs are reliable and can be utilized to simply calculate the structural downburst-induced vibration response. The results obtained can serve as a reference for the downburst-resistant design of long-span roof structures.

Keywords: downburst; long-span roof structure; downburst-induced vibration response; downburst-induced vibration coefficient (DVC); downburst-resistant design

Citation: Chen, C.; Huo, L.; Wang, Z.; Li, H. Downburst-Induced Vibration Coefficient of Long-Span Roof Structures. *Buildings* **2022**, *12*, 920. https://doi.org/10.3390/buildings12070920

Academic Editor: Vitor Silva

Received: 20 May 2022
Accepted: 24 June 2022
Published: 29 June 2022

1. Introduction

As sudden severe wind disasters, downbursts are defined as strong downdrafts that typically occur and descend from thunderstorm systems, and further induce outbursts of damaging winds on or near the ground. Downbursts have received much attention owing to their destructive power against affected structures [1–3]. The vertical wind profile of a downburst differs significantly from that of atmospheric boundary layer (ABL) wind. Additionally, the vertical wind speed, usually neglected in the ABL wind field, has strong effects on the characteristics of the downburst wind field [4]. Surveys and statistics show that frequent and widespread downbursts, especially microbursts, have caused considerable damage to aviation industries and civil infrastructures in recent decades [5–7]. Downbursts can pose severe threats to structures located in their impact areas [8–10]. Primary and enclosure structures exposed to a downburst can be seriously damaged.

As regional and even national landmarks, long-span roof structures (e.g., flat, saddle, cylindrical and spherical roof shapes) have been widely applied in stadiums, exhibition halls and shopping malls because of their excellent mechanical properties, large available space and graceful appearance [11–14]. However, these structures are wind-sensitive due to their low mass, high flexibility and small damping ratio, and tend to experience large vibrations and deformations under wind load excitation [15]. Therefore, researchers have focused on analyzing the wind-induced vibration response of long-span roof structures. Su et al. [16] presented a fast frequency-domain algorithm to evaluate the structural vibration response due to wind loads. The accuracy and efficiency of the new algorithm were verified via two case studies, including a long-span roof with a rise–span ratio of 1/3. Through wind tunnel tests, Wang et al. [17] measured wind pressure time histories and used the finite particle method (FPM) to evaluate the vibration response of a long-span roof. Their results demonstrated the reliability of the FPM in analyzing the response of such structures. Li et al. [18] systematically studied the non-stationarity of a tornado and its influence on the dynamic response of a long-span dome-roof structure through finite element analysis (FEA) and computational fluid dynamics (CFD) simulation. The results showed that when the tornado's core radius was close to the dome-roof structure, the non-stationary wind pressure and structural response became especially significant. Chen et al. [19] carried out full-scale measurements of the wind loads and vibration responses of a long-span roof structure during the typhoon Nuri. The measured response was compared with the FEA results. Moreover, likely inspired by the effective application of the wind-induced vibration coefficient (WVC) in high-rise structures [20], scholars investigated the WVC of long-span roof structures subjected to ABL wind loads. Research reported by He et al. [21], Zhang et al. [22] and Zhou et al. [23] proved that structural parameters, including geometry, damping ratio, roof mass and boundary conditions, can greatly influence the vibration responses of long-span roof structures. Hence, it is critical to comprehensively consider these parameters in a structural WVC analysis.

It should be noted that all of the above studies focus on long-span roof structures subjected to ABL wind, typhoon and tornado loads. However, because of the unique nature of downburst wind loads, the conventional WVC based on ABL wind loads is unsuitable for structures subjected to downbursts. Therefore, additional studies have been performed particularly to gain a better understanding of the downburst-induced vibration responses of long-span roof structures. Through the use of an improved deterministic–stochastic hybrid model, Chen et al. [24] presented a new method to numerically simulate the wind pressure and compute the microburst-induced response of a flat roof. They found that the ratio of the jet speed to translation speed of a microburst significantly influenced the peak value of the structural wind pressure. Another study performed a nonlinear analysis of the downburst-induced response of roof structures with force-limiting devices. The research showed that the reasonable application of force-limiting devices can reduce structural displacement and thus prevent the structure from collapsing [25]. Their research mainly focused on the structural dynamic response and did not analyze the impacts of structural parameters. Later, Zhou et al. [26] performed a parametric analysis of the downburst-induced vibration response of a simply supported beam roof structure. The influences of structural parameters, including stiffness and span, on the structural response were studied.

Current limited research on how downbursts affect long-span roof structures is focused primarily on the structural dynamic response and lacks comprehensive consideration of potential influencing parameters. In addition, there is even less research on the downburst-resistant design of such structures. This paper proposes the downburst-induced vibration coefficient (DVC), and presents a detailed study on the downburst-induced vibration response and DVC of a single-layer spherical reticulated structure. The influences of different parameters on the structural vibration response are first analyzed through the simulation of downbursts. Then, from the perspective of a statistics-guided downburst-resistant design, design DVCs of displacement and internal force are further proposed. Regression models that consider the influences of structural parameters are developed through an orthogonal analysis to assist in the design DVCs. Finally, the accuracy and reliability of the regression models are verified via the application to a case study.

2. Downburst Wind Field

According to the deterministic–stochastic hybrid model [27,28], the total wind speed of a downburst can be expressed as follows:

$$U(z,t) = \overline{U}(z,t) + u(z,t) \tag{1}$$

where $U(z,t)$ and $u(z,t)$ are the total wind speed and fluctuating component, respectively; $\overline{U}(z,t)$ is the time-varying mean wind speed, and can be expressed as follows:

$$\overline{U}(z,t) = V(z) \times f_{\mathrm{t}}(t) \tag{2}$$

in which $f_{\mathrm{t}}(t)$ is a time function related to the time-variability of the mean wind speed; $V(z)$ is the vertical wind profile, and can be described by the Wood model [29]:

$$V(z) = 1.55(z/\delta)^{1/6} \cdot [1 - \mathrm{erf}(0.7z/\delta)] \cdot V_{\mathrm{max}} \tag{3}$$

where V_{max} is the maximum horizontal wind speed in the above profile; δ is the height where the wind speed reaches half of its maximum value; $\mathrm{erf}(x) = 2/\sqrt{\pi} \cdot \int_0^x e^{-y^2} \mathrm{d}y$ is the error function.

Holmes et al. [30] pointed out that the actual wind speed of a downburst is approximately the vector synthesis of its radial speed and translation speed. Furthermore, the radial speed can be expressed as follows:

$$V_{\mathrm{r}}\,(r,t) = \begin{cases} V_{\mathrm{r,max}} \cdot (r/r_{\mathrm{max}}) & (r < r_{\mathrm{max}}) \\ V_{\mathrm{r,max}} \cdot \exp\left[-\left(\frac{r - r_{\mathrm{max}}}{R_{\mathrm{r}}}\right)^2\right] & (r \geq r_{\mathrm{max}}) \end{cases} \tag{4}$$

in which r is the horizontal distance between the observation point and the downburst center; $V_{\mathrm{r,max}}$ is the maximum wind speed; r_{max} is the horizontal distance between the radial position of $V_{\mathrm{r,max}}$ and the downburst center; R_{r} is the radial length scale.

As shown in Figure 1, the downburst of interest moves forward with a translation speed V_{r}. The initial coordinate of the observation point P relative to the downburst center O is set to (d_1, d_2). As the downburst moves, the above coordinate is updated to $(d_1 - V_{\mathrm{t}}t, d_2)$ at time t. Hence, the radial speed vector $V_{\mathrm{r}}(t)$ of the observation point can be obtained by:

$$V_{\mathrm{r}}(t) = \mathrm{r}/|\mathrm{r}| \cdot V_{\mathrm{r}}(|\mathrm{r}|, t) \tag{5}$$

in which $\mathrm{r} = (d_1 - V_{\mathrm{t}}t, d_2)$; $V_{\mathrm{r}}(\cdot)$ is the function of the radial speed as expressed by Equation (4).

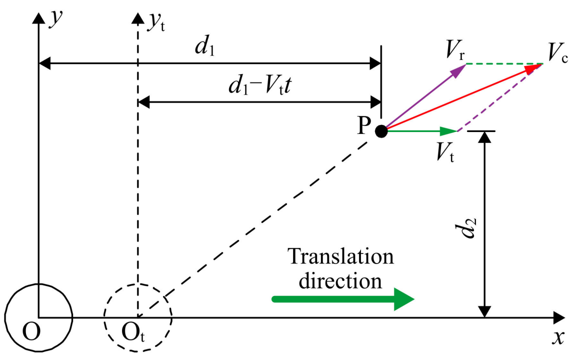

Figure 1. Vector synthesis of the downburst's radial speed and translation speed.

Then, the actual wind speed vector of the downburst can be written as follows:

$$V_{\mathrm{c}}(t) = V_{\mathrm{r}}(t) + V_{\mathrm{t}} \tag{6}$$

where $V_{\mathrm{t}} = (V_{\mathrm{t}}, 0)$ is the translation speed vector.

In this study, the variation of the wind direction caused by the downburst's translation is neglected; then, the time function $f_{\mathrm{t}}(t)$ in Equation (2) can be expressed as follows:

$$f_{\mathrm{t}}(t) = |V_{\mathrm{c}}(t)| / |V_{\mathrm{c}}(t)|_{\max} \tag{7}$$

Finally, the mean wind speed $\overline{U}(z,t)$ can be successfully obtained by substituting Equations (3) and (7) into Equation (2).

The fluctuating component of a downburst can be expressed as follows [28]:

$$u(z,t) = a(z,t) \cdot k(z,t) \tag{8}$$

in which $a(z,t) = 0.11\overline{U}(z,t)$ is a time-varying amplitude modulation function; $k(z,t)$ is a non-stationary stochastic process with a given power spectrum, and it reflects the characteristics of the fluctuating wind speed.

The following normalized Kaimal spectrum $S(z,w)$ is selected as the target power spectral density (PSD) of $k(z,t)$ [31]:

$$S(z,\omega) = \frac{1}{2}\frac{200}{2\pi}u_*^2\frac{z}{\overline{U}(z)}\frac{1}{\left[1+\dfrac{50z\omega}{2\pi\overline{U}(z)}\right]^{5/3}} \tag{9}$$

where $u_* = 1.76\ \mathrm{m/s}$ is the flow shear speed; ω is the circular frequency.

3. Methodology of Numerical Analysis

3.1. Analysis Method and Basic Assumptions

Considering that both the mean and fluctuating components of a downburst are time-varying, the Newmark-β method [32], which is a well-known time-domain analysis method, is utilized to obtain the structural dynamic response. In addition, compared with the size of a downburst wind field, the structural size is relatively small. Then, the following conditions are assumed:

(1) The effect of transverse turbulence, which is perpendicular to the wind flow direction, is ignored in the downburst wind field. That is to say, only the along-wind load is considered.

(2) The structural elements are in a linear elastic state for the duration of the downburst wind load, so as to guarantee the complete linear constitutive relation of the structural materials.

3.2. Downburst-Induced Vibration Coefficient (DVC)

Like the WVC applied to ABL wind loads, the structural dynamic effect caused by the fluctuating component of a downburst can be considered via DVC, which is defined here as the ratio of the total response to the mean response of the structure subjected to downbursts. Additionally, since the nodal displacement and elemental internal force are generally major considerations in the vibration response analysis of long-span roof structures, DVCs of nodal displacement and elemental internal force are adopted in this study.

In the conventional vibration response analysis of structures subjected to ABL wind loads, the peak assurance factor [23,33], which is a constant introduced to guarantee safety, is essential for the calculation of the WVC. However, there is still no reliable peak assurance factor for downburst wind loads. Furthermore, the time-variability of the mean wind speed of a downburst also means that the traditional approach to calculating the WVC, which is dependent on an invariant mean wind speed, is no longer suitable for downburst wind loads. Therefore, with the maximum structural response taken into consideration, the adopted DVCs of nodal displacement and elemental internal force in this study are defined as follows:

$$\begin{cases} \varphi_{\mathrm{D}i} = R_{\mathrm{D}i}/\overline{R}_{\mathrm{D}i} \\ \varphi_{\mathrm{F}j} = R_{\mathrm{F}j}/\overline{R}_{\mathrm{F}j} \end{cases} \tag{10}$$

where $\varphi_{\mathrm{D}i}$ and $\varphi_{\mathrm{F}j}$ are the DVCs of node i and element j, respectively; $R_{\mathrm{D}i}$ and $\overline{R}_{\mathrm{D}i}$ are the maximum displacements of node i under the total and mean downburst wind loads, respectively; $R_{\mathrm{F}j}$ and $\overline{R}_{\mathrm{F}j}$ are the maximum internal forces of element j under the total and mean downburst wind loads, respectively.

4. Numerical Analysis

4.1. Structural Model

A long-span single-layer spherical reticulated structure was selected for analysis. The structure was modeled in the working environment of MATLAB software by using the finite element method. As shown in Figure 2a, three-way hinged supports are set at the outermost nodes of the structure. Its eaves height is 10 m, and the cross-sectional size of the structural element is Φ132 mm × 5 mm. The elements are linked through rigid connections.

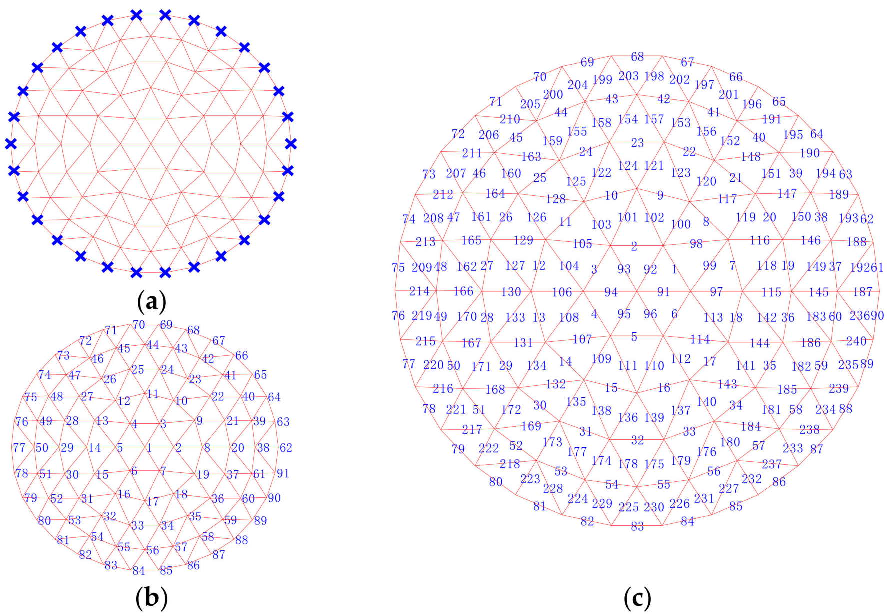

Figure 2. Long-span single-layer spherical reticulated structure: (**a**) structural model (top view); (**b**) node numbers; (**c**) element numbers.

Moreover, for the convenience of the following expression, a baseline model is defined. Its span (L), rise–span ratio (λ) and damping ratio (ζ) are 40 m, 1/5 and 0.03, respectively. Furthermore, the roof mass (W), uniformly distributed on the structure, is 80 kg/m^2. There are 91 nodes and 240 elements in total, and the node numbers and element numbers are presented in Figure 2b,c.

4.2. Simulation of Downbursts

According to the theory presented in Section 2, downburst wind speeds at the structural nodes were further simulated. Considering that downbursts are generally characterized by their short life span (approximately 10 to 20 min) but high-intensity winds [9], and that a large number of simulations were carried out in this study, a simulation time of T = 600 s was selected. The downburst's translation speed was set to V_{t} = 10 m/s, and the relative position coordinate of the structural vertex to the downburst center at time t = 0 was specified as (d_1,d_2) = (3000 m, 150 m). The other simulation parameters adopted are listed in Table 1 [27,30], where the parameter values are set according to the aforementioned Wood model and the vector synthesis method.

Table 1. Main parameters adopted in the simulation of downbursts.

Parameter	V_{max}(m/s)	δ(m)	$V_{r,max}$(m/s)	R_r(m)	r_{max}(m/s)
Value	80	400	47	700	1000

Figure 3 shows the simulated downburst at node 9 on the baseline model. It is obvious from Figure 3a that the time function well reflects the variation of the mean wind speed. In addition, the comparison of PSDs, displayed in Figure 3d, shows that the simulated PSD was consistent with the target one, indicating the reliable simulation of the fluctuating wind speed.

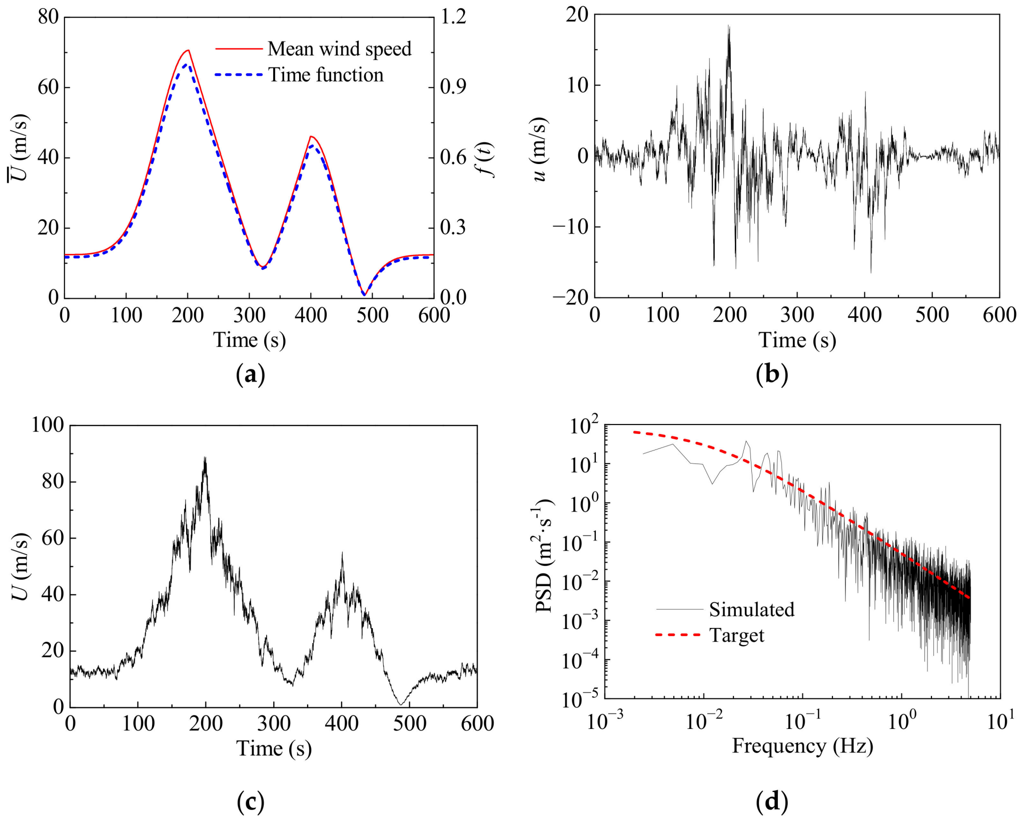

Figure 3. Simulated downburst at node 9: (**a**) mean wind speed and time function; (**b**) fluctuating wind speed; (**c**) total wind speed; (**d**) comparison of the PSDs.

4.3. Influences of the Structural Parameters

In this section, the influences of the parameters described in Section 4.1 on the structural vibration response are discussed in detail. Considering the practical engineering application and that it is inadvisable for a single-layer spherical reticulated structure with a span over 80m or a rise–span ratio of less than 1/7 [34], parameter values of the structure are set and listed in Table 2.

Table 2. Parameter values of the structure.

Parameter	L(m)			λ			ζ			W (kg/m^2)		
Value	30	40	50	1/6	1/5	1/4	0.01	0.03	0.05	40	80	120

In the following analysis, the roof mass is concentrated to the structural nodes. Moreover, it should be noted that when investigating the influence of a certain parameter, the other parameters are kept constant and the same as those of the baseline model. Due to the randomness of downburst wind loads, each possible parameter combination requires numerous simulations in order to allow for proper statistical analysis and the discovery of any trends in the structural response. Furthermore, due to the geometric symmetry of the structure and for convenience, a group of radial nodes and elements located at the structural symmetrical position was representatively selected for analysis. The fluctuations in the nodal displacements and elemental internal forces are described by their mean square deviations, which can be obtained from:

$$\begin{cases} \sigma_{\mathrm{D}i} = \sqrt{\dfrac{1}{n-1}\sum\limits_{i=1}^{n}\left(D_i - \overline{D}_i\right)^2} \\ \sigma_{\mathrm{F}j} = \sqrt{\dfrac{1}{n-1}\sum\limits_{j=1}^{n}\left(F_j - \overline{F}_j\right)^2} \end{cases} \tag{11}$$

where D_i, $\overline{D}_i$ and σ_{Di} are the total, mean and mean square vertical displacements of node i, respectively; F_j, $\overline{F}_j$ and σ_{Fj} are the total, mean and mean square internal forces of element j, respectively; n is the number of load steps.

Figure 4 shows the structural responses versus different spans. It was observed that with the increase of span, the mean and fluctuation of the nodal displacements and elemental internal forces increase synchronously. This synchronicity arises from the fact that increasing the span decreases of the structural stiffness. In addition, the DVCs of nodal displacement and elemental internal force also increase gradually with the increasing span.

The relationship between the structural response and the rise–span ratio is shown in Figure 5, where the mean and fluctuating responses of nodal displacement and elemental internal force both decrease with the increasing rise–span ratio. This phenomenon occurs because the increasing rise–span ratio increases the structural stiffness. In addition, Figure 5e shows that for nodes at the middle of the structure, increasing rise–span ratio decreases the DVC of nodal displacement. However, for nodes near the structural edge, the DVC of nodal displacement increases with the increasing rise–span ratio. This is because the non-uniform distribution of the wind pressure on the structural surface leads to the corresponding differences of wind sensitivity at different regions of the structure. As the rise–span ratio increases, the nodal displacements near the structural edge form a multi-wave surface under the action of the fluctuating load. However, the mean displacements of these nodes are relatively small due to the constraints. Additionally, according to the definition of the DVC of nodal displacement, the ratios of the total displacements to the mean displacements increase for these nodes but remain within a reasonable range. Moreover, nodes with an abnormal DVC of nodal displacement are located near the roof edge and obviously unable to serve as controlling factors to guarantee structural safety. Finally, as shown in Figure 5f, the DVC of elemental internal force decreases gradually with the increasing rise–span ratio, which is consistent with the behavior of elemental internal force.

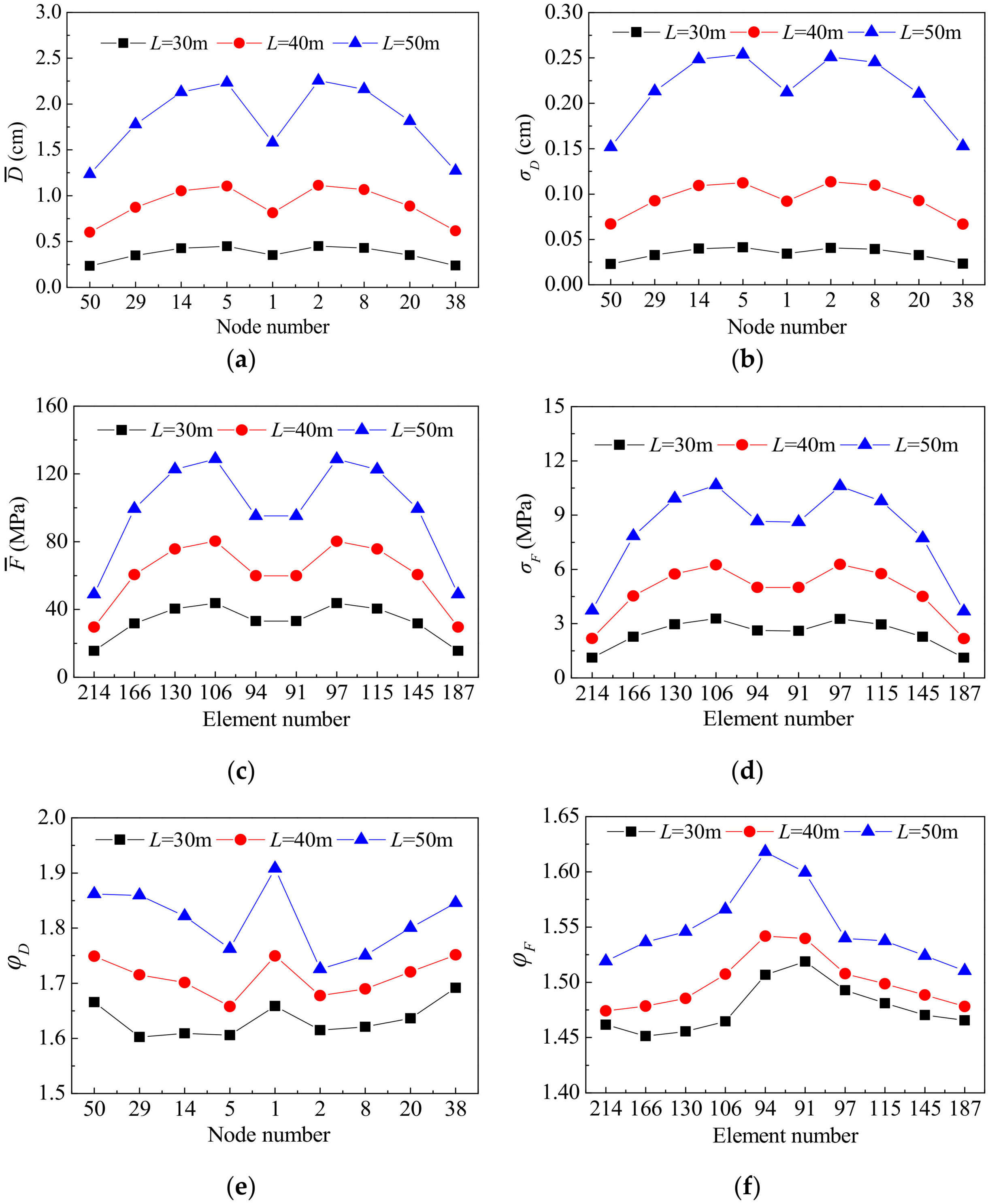

Figure 4. Structural responses versus different spans: (**a**) mean displacements of nodes; (**b**) mean square displacements of nodes; (**c**) mean internal forces of elements; (**d**) mean square internal forces of elements; (**e**) DVCs of nodal displacement; (**f**) DVCs of elemental internal force.

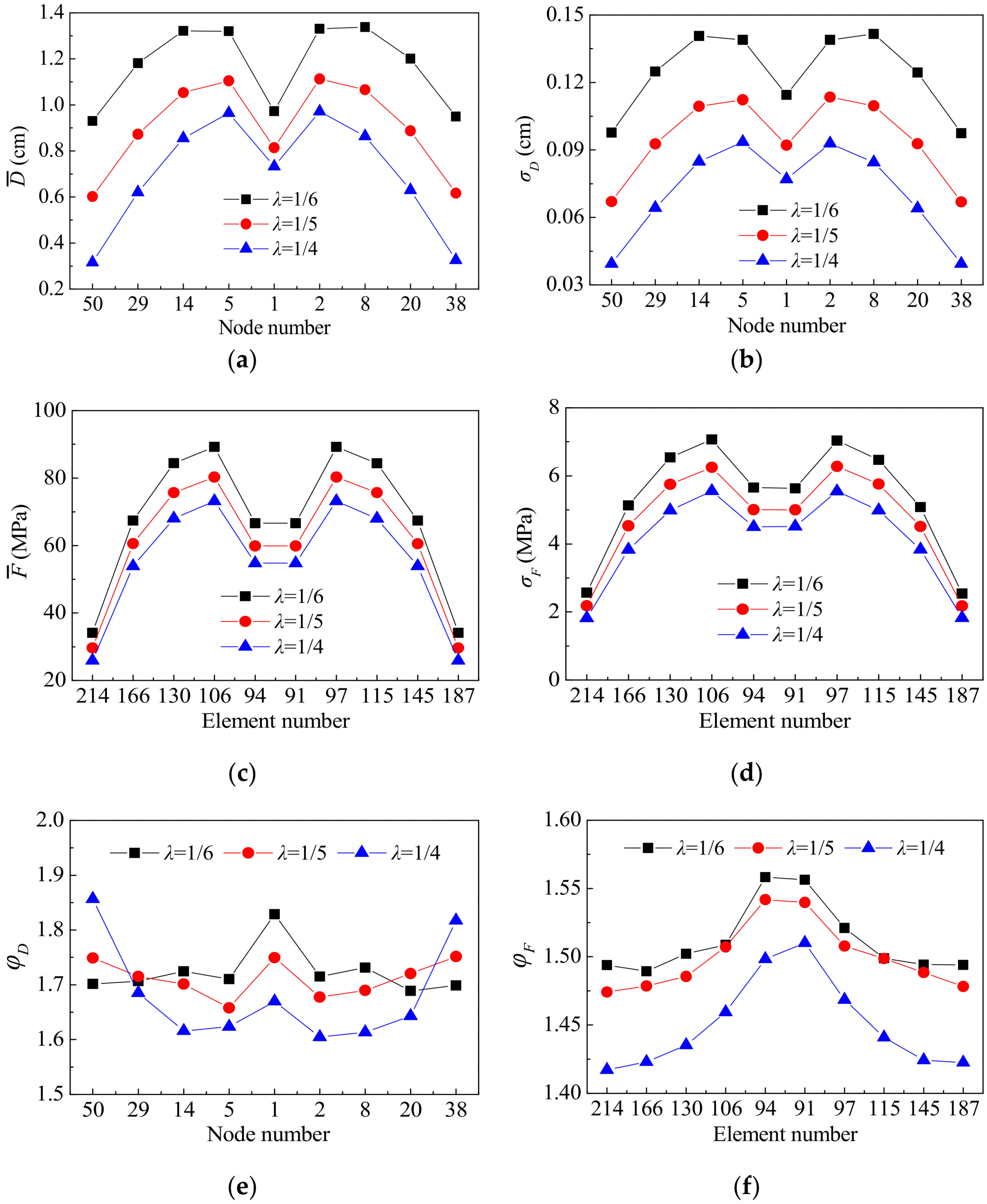

Figure 5. Structural responses versus different rise–span ratios: (**a**) mean displacements of nodes; (**b**) mean square displacements of nodes; (**c**) mean internal forces of elements; (**d**) mean square internal forces of elements; (**e**) DVCs of nodal displacement; (**f**) DVCs of elemental internal force.

Figure 6 shows that the damping ratio can hardly affect the mean structural response because the mean component of the downburst wind load varies slowly enough to be nearly equivalent to a static process. However, as the damping ratio increases, the fluctuations of the nodal displacement and elemental internal force both decrease, especially when the damping ratio increases from 0.01 to 0.03. Moreover, the DVCs of nodal displacement and elemental internal force also decrease with the increasing damping ratio.

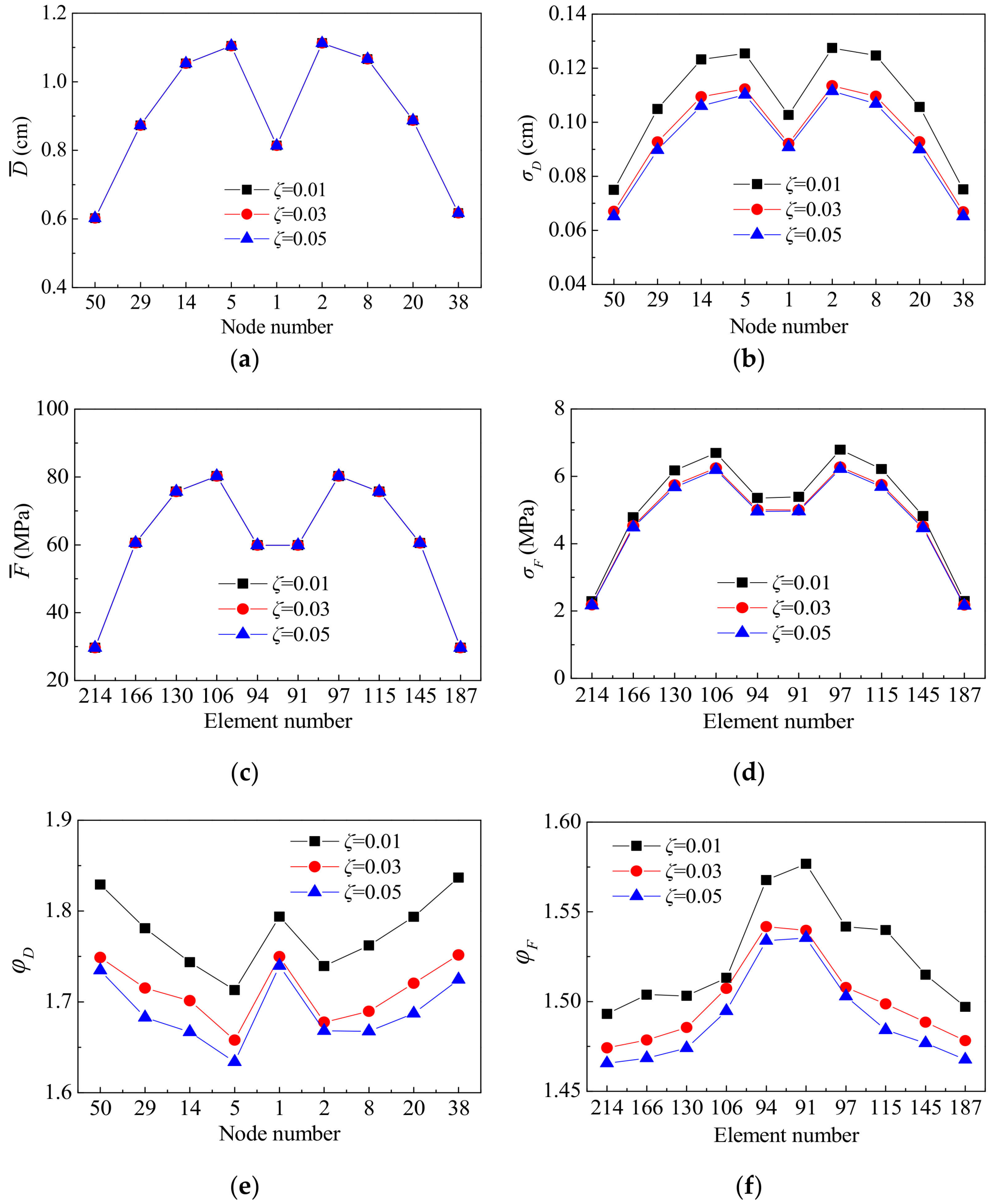

Figure 6. Structural responses versus different damping ratios: (**a**) mean displacements of nodes; (**b**) mean square displacements of nodes; (**c**) mean internal forces of elements; (**d**) mean square internal forces of elements; (**e**) DVCs of nodal displacement; (**f**) DVCs of elemental internal force.

Figure 7 displays the structural responses versus different roof masses. As in the case above, the slow variation of the mean component of the downburst wind load means that the change of roof mass has little influence on the mean responses. However, with the increase of roof mass, the structural frequency decreases and becomes closer to the frequency of the downburst wind load, and thus increases the fluctuations of the nodal displacements and elemental internal forces. Moreover, it is clear from Figure 7e,f that the DVCs of nodal displacement and elemental internal force increase with the increasing roof mass, which is parallel to the relationship between the mean and fluctuating responses.

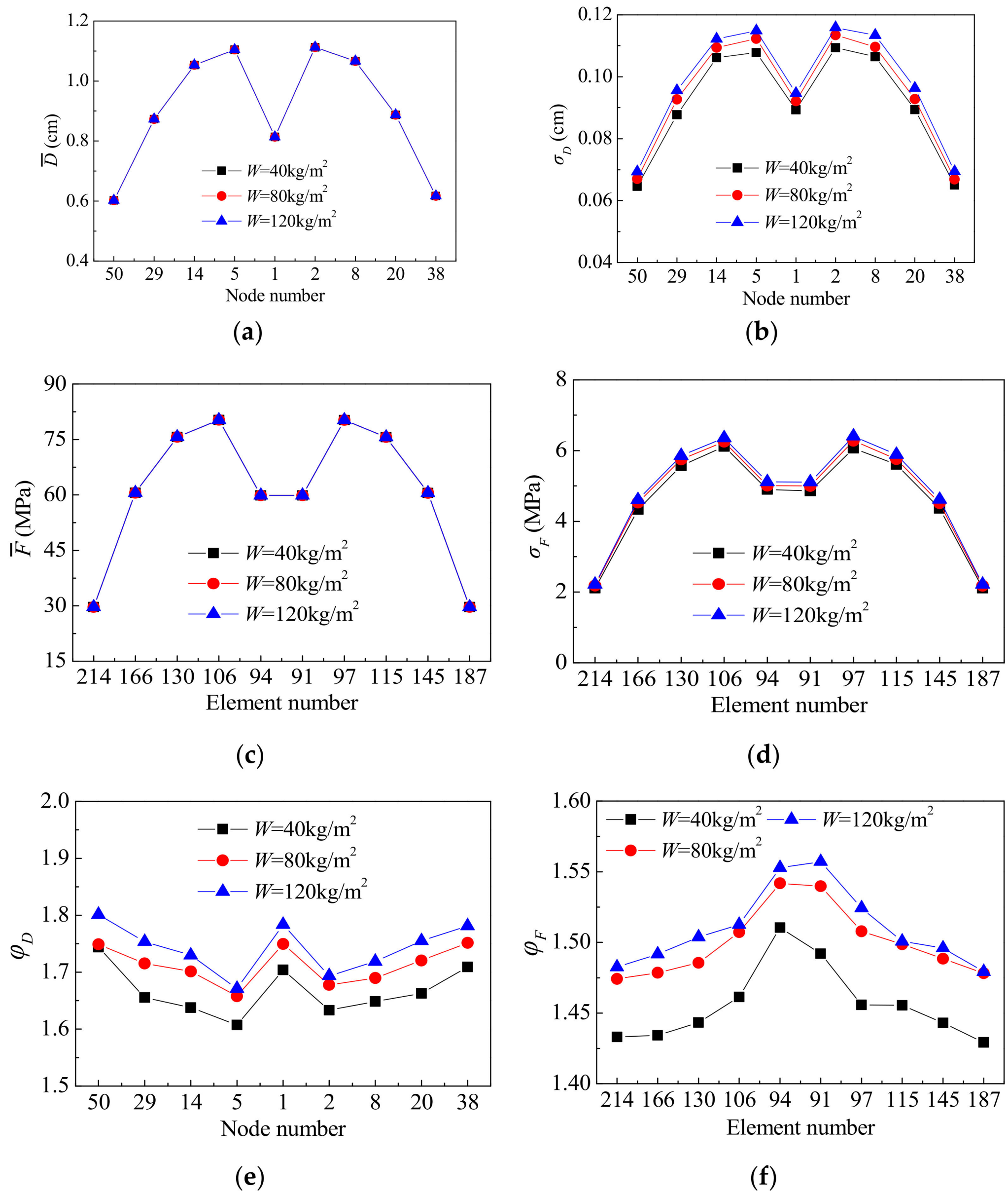

Figure 7. Structural responses versus different roof masses: (**a**) mean displacements of nodes; (**b**) mean square displacements of nodes; (**c**) mean internal forces of elements; (**d**) mean square internal forces of elements; (**e**) DVCs of nodal displacement; (**f**) DVCs of elemental internal force.

4.4. Global DVC of the Structure

Long-span roof structures typically require numerous nodes and elements for modeling with adequate accuracy. Furthermore, their DVCs are dissimilar. Hence, it is impractical for engineers to evaluate the safety of the whole structure according to the DVC of each node or element. Therefore, borrowing the idea of envelope [23], the following global DVCs are introduced to capture the total responses of all nodes and elements:

$$\begin{cases} \varphi_{\mathrm{D}}^{*} = \left\{\varphi_{\mathrm{D}i} \times \left|\overline{D}_i\right|\right\}_{\max} / \left\{\left|\overline{D}_i\right|\right\}_{\max} \\ \varphi_{\mathrm{F}}^{*} = \left\{\varphi_{\mathrm{F}j} \times \left|\overline{F}_j\right|\right\}_{\max} / \left\{\left|\overline{F}_j\right|\right\}_{\max} \end{cases} \tag{12}$$

where φ_{D}^{*} and φ_{F}^{*} are the global DVCs of displacement and internal force, respectively; $\left\{\varphi_{\mathrm{D}i} \times \left|\overline{D}_i\right|\right\}_{\max}$ is the structural maximum nodal displacement due to the total downburst wind load, $\left\{\left|\overline{D}_i\right|\right\}_{\max}$ is the maximum displacement of the corresponding node due to the mean downburst wind load; $\{\varphi_{Fj} \times |\overline{F}_j|\}_{max}$ is the structural maximum elemental internal force due to the total downburst wind load; $\{|\overline{F}_j|\}_{max}$ is the maximum internal force of the corresponding element caused by the mean downburst wind load.

As shown in Figures 8 and 9, analyzing the vibration response of the baseline model reveals that the DVCs of nodal displacement and elemental internal force are extremely non-uniform. And for quite a few nodes and elements, the DVCs are greater than their corresponding global DVC. However, the computed results demonstrate that these nodes and elements with greater DVCs tend to have relatively smaller responses, implying that they can hardly control structural safety. Finally, it is clear that these nodes with DVCs greater than the corresponding global DVC are primarily located near the structural constraints, which can also be explained as described in Section 4.3.

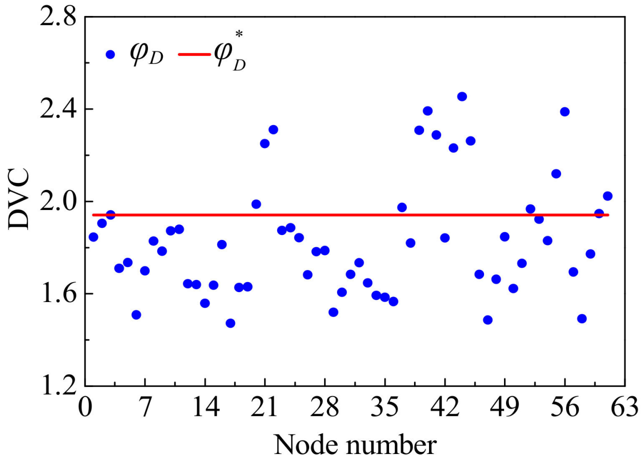

Figure 8. Comparison of the DVC of nodal displacement and the global DVC of displacement.

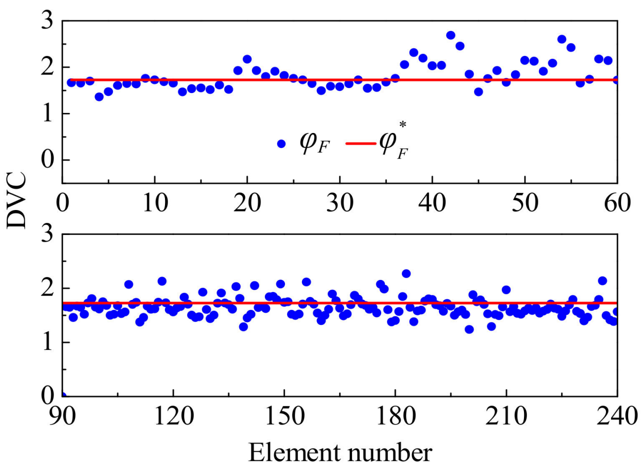

Figure 9. Comparison of the DVC of elemental internal force and the global DVC of internal force.

Figure 10 compares the actual total responses and those computed via the global DVCs for the baseline model. It can be found that the computed total responses effectively envelope the actual responses. For a portion of nodes and elements, the computed total response is lower than the actual response; however, the structure is still safe according to the actual maximum nodal displacement ($(R_D)_{max}$, as shown in Figure 10a) and elemental internal force ($(R_F)_{max}$, as shown in Figure 10b), which are equal to the computed maximum values.

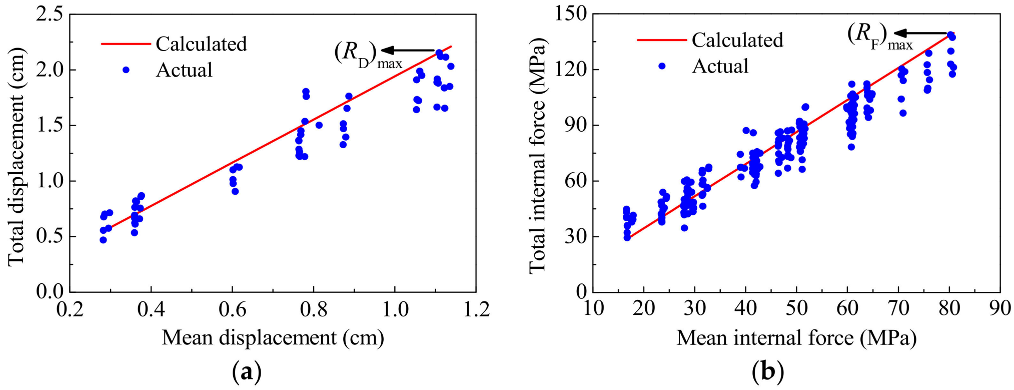

Figure 10. Comparisons of the structural total responses: (**a**) nodal displacement; (**b**) elemental internal force.

Figure 11 reveals the influences of structural parameters on the global DVCs of displacement and internal force. It is clear that the global DVCs increase with the increasing span and roof mass, and decrease with the increasing rise–span ratio and damping ratio. Such behavior is consistent with the DVCs of nodal displacement and elemental internal force.

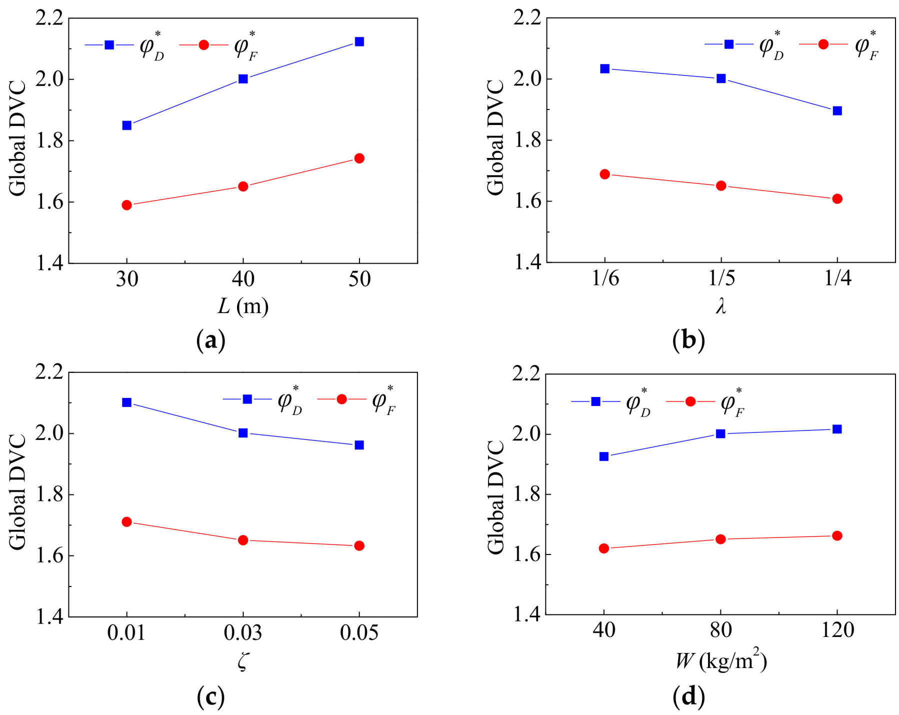

Figure 11. Influences of structural parameters on the global DVCs: (**a**) span; (**b**) rise–span ratio; (**c**) damping ratio; (**d**) roof mass.

4.5. Results and Discussion

Based on the previous analysis, it is clear that the structural responses are affected by multiple parameters, among which the span and rise–span ratio have larger influences than the damping ratio and roof mass. Specifically, the structural responses increase with the increasing span and roof mass, while decrease with the increasing rise–span ratio and damping ratio. Damping ratio and roof mass primarily affect the fluctuating responses. Furthermore, the influences of the structural parameters on the global DVCs of displacement and internal force are consistent with that of the DVCs of nodal displacement and elemental internal force.

The DVCs of nodal displacement and elemental internal force are obviously discrete, and the proposed computational method based on the global DVCs provides a more efficient way to acquire the total responses of the whole structure with the precondition of ensuring safety.

5. Design DVC of the Structure

The randomness of downburst wind loads means that the uncertainty of the global DVCs obtained from Equation (12) hinders the direct use of the global DVCs for the downburst-resistant design of long-span roof structures. Considering that numerous calculations are performed for statistical analysis, the above global DVCs meet the characteristics of normal distribution, and can be further characterized by

$$\begin{cases} \dfrac{\varphi_{\mathrm{D}}^{*} - \mu(\varphi_{\mathrm{D}}^{*})}{\sigma(\varphi_{\mathrm{D}}^{*})} \sim N(0,1) \\ \dfrac{\varphi_{\mathrm{F}}^{*} - \mu(\varphi_{\mathrm{F}}^{*})}{\sigma(\varphi_{\mathrm{F}}^{*})} \sim N(0,1) \end{cases} \tag{13}$$

where $\mu(\varphi_{\mathrm{D}}^{*})$ and $\sigma(\varphi_{\mathrm{D}}^{*})$ are the mean and mean square values of the global DVC of displacement, respectively; $\mu(\varphi_{\mathrm{F}}^{*})$ and $\sigma(\varphi_{\mathrm{F}}^{*})$ are the mean and mean square values of the global DVC of internal force, respectively.

Therefore, the following design DVCs, which consider the statistical characteristics and include the design DVC of displacement Φ_{D} and design DVC of internal force Φ_{F}, are further proposed:

$$\Phi_{\mathrm{D}} \begin{cases} \Phi_{\mathrm{D}} = \mu(\varphi_{\mathrm{D}}^{*}) + \alpha\sigma(\varphi_{\mathrm{D}}^{*}) \\ \Phi_{\mathrm{F}} = \mu(\varphi_{\mathrm{F}}^{*}) + \alpha\sigma(\varphi_{\mathrm{F}}^{*}) \end{cases} \tag{14}$$

where α, the safety coefficient, is set to 2.06 based on mathematical statistics to provide a safety assurance rate of 98%.

Then, in the downburst-resistant design of long-span roof structures, the total structural responses can be estimated by

$$\begin{cases} R_{\mathrm{D}} = \Phi_{\mathrm{D}}\overline{R}_{\mathrm{D}} \\ R_{\mathrm{F}} = \Phi_{\mathrm{F}}\overline{R}_{\mathrm{F}} \end{cases} \tag{15}$$

where R_{D} and $\overline{R}_{\mathrm{F}}$ are the structural displacement and internal force under the total downburst wind load, respectively; $\overline{R}_{\mathrm{D}}$ and $\overline{R}_{\mathrm{F}}$ are the displacement and internal force under the mean downburst wind load, respectively.

5.1. Orthogonal Calculation and Regression Analysis

It should be noted that the structural response is affected by multiple parameters. Therefore, using the concept of the orthogonal test [35], a series of orthogonal calculations were carried out in the following to consider all potential influences of different parameters on the proposed design DVCs. Calculation cases were formulated according to the analysis in Section 4.3 and listed in Table 3. A statistical analysis was also performed for each case, which comprises a large number of calculations.

Table 3. Orthogonal calculation cases.

Case No.	L (m)	λ	ζ	W (kg/m^2)	Case No.	L (m)	λ	ζ	W (kg/m^2)
1	44	0.22	0.04	100	16	37	0.195	0.03	80
2	30	0.22	0.02	100	17	37	0.195	0.03	120
3	37	0.195	0.03	40	18	37	0.195	0.03	80
4	44	0.17	0.02	100	19	30	0.17	0.04	60
5	30	0.22	0.02	60	20	44	0.22	0.02	100
6	37	0.195	0.03	80	21	30	0.17	0.02	100
7	37	0.245	0.03	80	22	51	0.195	0.03	80
8	44	0.22	0.02	60	23	23	0.195	0.03	80
9	37	0.195	0.05	80	24	44	0.17	0.04	60
10	30	0.17	0.04	100	25	37	0.195	0.03	80
11	30	0.17	0.02	60	26	37	0.195	0.03	80
12	37	0.195	0.03	80	27	37	0.195	0.01	80
13	30	0.22	0.04	100	28	44	0.22	0.04	60
14	44	0.17	0.04	100	29	37	0.145	0.03	80
15	44	0.17	0.02	60	30	30	0.22	0.04	60

The previous analysis shows that the structural response is nonlinearly influenced by different parameters. Hence, the following quadratic regression models are proposed to characterize the relationship between the design DVCs and the structural parameters:

$$\begin{cases} \Phi_{\mathrm{D}} = \eta_0 + \eta_1 L + \eta_2 \lambda + \eta_3 \zeta + \eta_4 W + \eta_{11} L^2 + \eta_{12} L\lambda + \eta_{13} L\zeta + \\ \quad \eta_{14} LW + \eta_{22}\lambda^2 + \eta_{23}\lambda\zeta + \eta_{24}\lambda W + \eta_{33}\zeta^2 + \eta_{34}\zeta W + \eta_{44} W^2 \\ \Phi_{\mathrm{F}} = \chi_0 + \chi_1 L + \chi_2 \lambda + \chi_3 \zeta + \chi_4 W + \chi_{11} L^2 + \chi_{12} L\lambda + \chi_{13} L\zeta + \\ \quad \chi_{14} LW + \chi_{22}\lambda^2 + \chi_{23}\lambda\zeta + \chi_{24}\lambda W + \chi_{33}\zeta^2 + \chi_{34}\zeta W + \chi_{44} W^2 \end{cases} \tag{16}$$

in which the parameters η and χ with subscripts are the regression coefficients.

Then, based on the results obtained from orthogonal calculations, significance analysis of the regression models was performed with Design-Expert software (Version 8.0.6.1), which has unique advantages in experimental design and data analysis [36]. Tables 4 and 5 show the preliminary significance analysis results of models Φ_{D} and Φ_{F}, respectively. The value of p is the significant index; in particular, $p \leq 0.01$, $p \leq 0.05$ and $p > 0.05$ mean that the corresponding source has extremely significant, significant and low influence on the model being analyzed, respectively.

Table 4. Preliminary significance analysis results of model Φ_{D}.

Source	Sum of Square	Degree of Freedom	Mean Square	p
L	3.4×10^{-1}	1	3.4×10^{-1}	<0.0001
λ	5.83×10^{-4}	1	5.83×10^{-4}	0.2878
ζ	1.5×10^{-2}	1	1.5×10^{-2}	<0.0001
W	7.48×10^{-3}	1	7.48×10^{-3}	0.0013
$L\lambda$	1.8×10^{-2}	1	1.8×10^{-2}	<0.0001
$L\zeta$	4.18×10^{-3}	1	4.18×10^{-3}	0.0099
LW	5.87×10^{-4}	1	5.87×10^{-4}	0.2864
$\lambda\zeta$	4.26×10^{-5}	1	4.26×10^{-5}	0.7698
ζW	1.42×10^{-3}	1	1.42×10^{-3}	0.1055
λW	6.88×10^{-4}	1	6.88×10^{-4}	0.2499
L^2	3.71×10^{-3}	1	3.71×10^{-3}	0.014
λ^2	2.29×10^{-4}	1	2.29×10^{-4}	0.5001
ζ^2	3.04×10^{-3}	1	3.04×10^{-3}	0.0237
W^2	2.39×10^{-4}	1	2.39×10^{-4}	0.4914

Table 5. Preliminary significance analysis results of model Φ_F.

Source	Sum of Square	Degree of Freedom	Mean Square	*p*
L	1.7×10^{-1}	1	1.7×10^{-1}	<0.0001
λ	7.05×10^{-4}	1	7.05×10^{-4}	0.3597
ζ	7.44×10^{-3}	1	7.44×10^{-3}	0.0078
W	4.53×10^{-3}	1	4.53×10^{-3}	0.0301
$L\lambda$	1.6×10^{-2}	1	1.6×10^{-2}	0.0005
$L\zeta$	1×10^{-2}	1	1×10^{-2}	0.0026
LW	1.21×10^{-6}	1	1.21×10^{-6}	0.9694
$\lambda\zeta$	5.21×10^{-4}	1	5.21×10^{-4}	0.4293
ζW	8.48×10^{-4}	1	8.48×10^{-4}	0.3162
λW	6.11×10^{-4}	1	6.11×10^{-4}	0.3928
L^2	9.21×10^{-5}	1	9.21×10^{-5}	0.7373
λ^2	3.42×10^{-4}	1	3.42×10^{-4}	0.5204
ζ^2	1.55×10^{-3}	1	1.55×10^{-3}	0.1819
W^2	2.44×10^{-3}	1	2.44×10^{-3}	0.0988

Parameters and product terms with $p > 0.05$ were ignored and then the model corresponding to them was reanalyzed. After several rounds of analysis, the final significance analysis results of models Φ_D and Φ_F were obtained, as respectively shown in Tables 6 and 7. It can be found that parameters L, ζ and W and product terms $L\lambda$ and $L\zeta$ have non-negligible influences on the design DVCs. In addition, $p > 0.05$ for the item "Lack of fit" in the two models indicates an insignificant mismatch of the regression models. Meanwhile, $p < 0.0001$ for the item "Model" in the two models validates the reliability of the regression results.

Table 6. Final significance analysis results of model Φ_D.

Source	Sum of Square	Degree of Freedom	Mean Square	*p*
Model	3.9×10^{-1}	5	7.8×10^{-2}	<0.0001
L	3.4×10^{-1}	1	3.4×10^{-1}	<0.0001
ζ	1.5×10^{-2}	1	1.5×10^{-2}	<0.0001
W	7.48×10^{-3}	1	7.48×10^{-3}	0.003
$L\lambda$	1.8×10^{-2}	1	1.8×10^{-2}	<0.0001
$L\zeta$	4.18×10^{-3}	1	4.18×10^{-3}	0.021
Lack of fit	1.5×10^{-2}	19	7.86×10^{-4}	0.1441

Table 7. Final significance analysis results of model Φ_F.

Source	Sum of Square	Degree of Freedom	Mean Square	*p*
Model	2×10^{-1}	5	4.1×10^{-2}	<0.0001
L	1.7×10^{-1}	1	1.7×10^{-1}	<0.0001
ζ	7.44×10^{-3}	1	7.44×10^{-3}	0.0049
W	4.53×10^{-3}	1	4.53×10^{-3}	0.0235
$L\lambda$	1.6×10^{-2}	1	1.6×10^{-2}	0.0002
$L\zeta$	1×10^{-2}	1	1×10^{-2}	0.0013
Lack of fit	1.4×10^{-2}	19	7.22×10^{-4}	0.7113

According to the above analysis, the final regression models of the design DVCs are obtained as follows:

$$\begin{cases} \Phi_D = 1.475 + 0.026L + 6.047\zeta + 8.827 \times 10^{-4}W - 9.705 \times 10^{-3}L\lambda - 0.231L\zeta \\ \Phi_F = 1.165 + 0.025L + 11.616\zeta + 6.87 \times 10^{-4}W - 9.869 \times 10^{-3}L\lambda - 0.362L\zeta \end{cases} \quad (17)$$

Figure 12 compares the design DVCs obtained via regression (i.e., Equation (17)) and those obtained through orthogonal calculations. It can be found that the design DVCs of both displacement and internal force closely follow an ideal straight line, on which the design DVCs obtained from regression are equal to those obtained from orthogonal calculations.

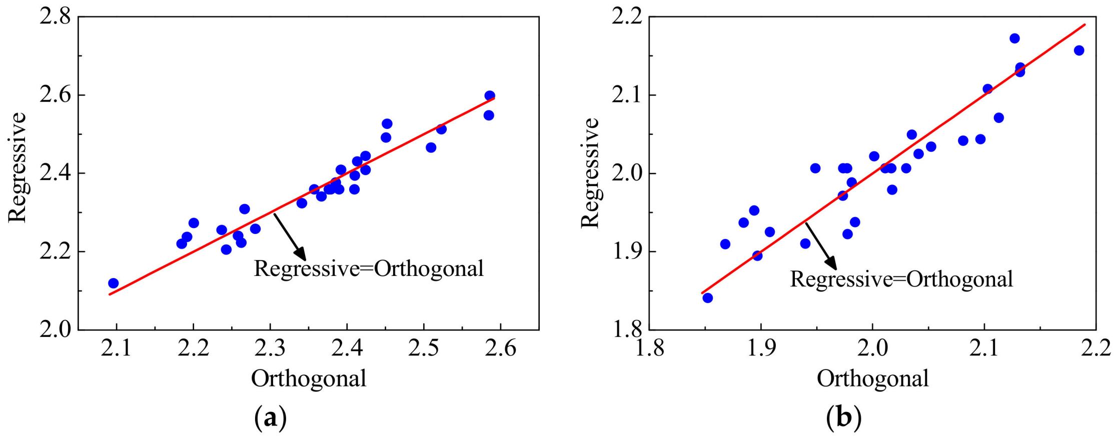

Figure 12. Comparisons of the design DVCs obtained via regression and orthogonal calculations: (**a**) design DVC of displacement; (**b**) design DVC of internal force.

5.2. A New Case Study

To further demonstrate the reliability of the above regression models, a structure with parameters $L = 38$ m, $\lambda = 1/7$, $\zeta = 0.02$ and $W = 70\ \mathrm{kg/m^2}$ was selected as the basis for a new case study. The proposed and actual total responses are compared in Figure 13, where the proposed total responses were obtained via the design DVCs calculated by Equation (17). It is obvious that the actual total responses are well within the envelope set by the proposed responses, especially for the nodes and elements with large responses.

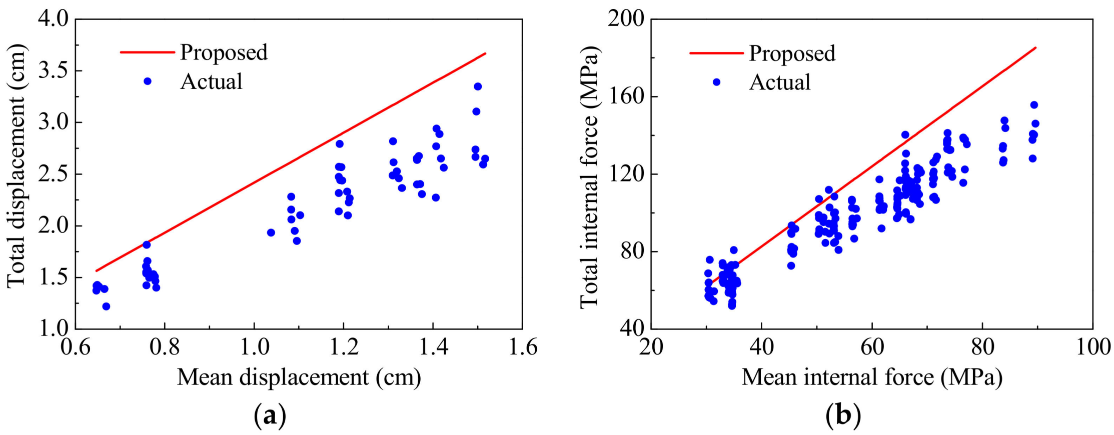

Figure 13. Comparisons of the proposed and actual total responses of the structure: (**a**) nodal displacement; (**b**) elemental internal force.

5.3. Discussion

Fully considering the randomness of downburst wind loads and the comprehensive influences of multi-structural parameters, design DVCs of displacement and internal force are proposed for providing a practicable way to evaluate the total structural response in the downburst-resistant design of long-span roof structures. In addition, the relationship between the design DVCs and the structural parameters can be characterized by quadratic polynomial regression models.

The comparison between the design DVCs obtained via regression and those obtained through orthogonal calculations verifies that the obtained regression models of the design

DVCs are sufficiently accurate to compute the design DVCs. In addition, the case study further demonstrates that the proposed regression models are reliable, and thus can be practically used to more efficiently evaluate the total response of long-span roof structures.

6. Conclusions

The threat of potentially catastrophic damage done to wind-sensitive structures has become a long-time topic of interest for researchers. However, there is not yet enough effort and attention directed towards studying and mitigating the impacts of downburst wind loads on long-span roof structures. In view of this situation, this paper performed a parametric study on the downburst-induced vibration response of a single-layer spherical reticulated structure and proposed the downburst-induced vibration coefficient (DVC). The main conclusions were as follows:

(1) The parametric studies show that the structural vibration responses (i.e., nodal displacements, elemental internal forces and their corresponding DVCs) generally increase with the increasing span and roof mass, and decrease with the increasing rise–span ratio and damping ratio. In addition, the damping ratio and roof mass have relatively little influence on the mean responses of nodal displacements and elemental internal forces.

(2) The design DVCs of displacement and internal force proposed in this study can sufficiently account for the randomness of downburst wind loads and make it possible to uniformly capture the total responses of all nodes and elements.

(3) The proposed regression models of the design DVCs of displacement and internal force are reliable enough to be practically used for civil engineers to more efficiently evaluate the total structural response in the downburst-resistant design of long-span roof structures.

Author Contributions: Conceptualization, L.H.; methodology, H.L.; software, C.C.; validation, L.H. and H.L.; formal analysis, L.H. and H.L.; investigation, C.C.; resources, Z.W.; data curation, C.C.; writing—original draft preparation, C.C.; writing—review and editing, L.H. and Z.W.; visualization, Z.W.; supervision, L.H.; project administration, L.H. and H.L.; funding acquisition, L.H. and H.L. All authors have read and agreed to the published version of the manuscript.

Funding: This research was co-funded by the National Key Research and Development Program of China, funding number 2016YFC0701103; the Dalian High Level Talent Innovation Support Program, funding number 2019RD01.

Institutional Review Board Statement: Not applicable.

Informed Consent Statement: Not applicable.

Data Availability Statement: Not applicable.

Conflicts of Interest: The authors declare no conflict of interest.

References

1. Solari, G.; Burlando, M.; De Gaetano, P.; Repetto, M.P. Characteristics of thunderstorms relevant to the wind loading of structures. *Wind Struct.* **2015**, *20*, 763–791. [CrossRef]
2. Wang, X.; Wang, J.H.; Miao, C.S.; Zeng, K. Forewarning method of downburst based on feature recognition and extrapolation. *Nat. Hazards* **2020**, *103*, 903–921. [CrossRef]
3. Wang, Z.S.; Yang, F.; Wang, Y.J.; Fang, Z.Y. Study on wind loads of different height transmission towers under downbursts with different parameters. *Buildings* **2022**, *12*, 193. [CrossRef]
4. Letchford, C.W.; Mans, C.; Chay, M.T. Thunderstorms-their importance in wind engineering (a case for the next generation wind tunnel). *J. Wind Eng. Ind. Aerodyn.* **2002**, *90*, 1415–1433. [CrossRef]
5. Fujita, T.T.; Byers, H.R. Spearhead echo and downburst in the crash of an airliner. *Mon. Weather Rev.* **1977**, *105*, 129–146. [CrossRef]
6. Pita, G.L.; de Schwarzkopf, M.L.A. Urban downburst vulnerability and damage assessment from a case study in Argentina. *Nat. Hazards* **2016**, *83*, 445–463. [CrossRef]
7. Loredo-Souza, A.M.; Lima, E.G.; Vallis, M.B.; Rocha, M.M.; Wittwer, A.R.; Oliveira, M.G.K. Downburst related damages in Brazilian buildings: Are they avoidable? *J. Wind Eng. Ind. Aerodyn.* **2019**, *185*, 33–40. [CrossRef]

8. Trautner, C.; Ojdrovic, R.; Schafer, B.W.; Jones, N.P. An investigation of the collapse of the Dallas Cowboys Practice Facility. In Proceedings of the Sixth Congress on Forensic Engineering, San Francisco, CA, USA, 31 October–3 November 2012.
9. Le, V.; Caracoglia, L. Computationally efficient stochastic approach for the fragility analysis of vertical structures subjected to thunderstorm downburst winds. *Eng. Struct.* **2018**, *165*, 152–169. [CrossRef]
10. Sengupta, A.; Haan, F.L.; Sarkar, P.P.; Balaramudu, V. Transient loads on buildings in microburst and tornado winds. *J. Wind Eng. Ind. Aerodyn.* **2008**, *96*, 2173–2187. [CrossRef]
11. Yan, J.W.; Peng, H.; Yu, Y.; Luo, Y.Z. Compressive sensing of wind speed based on non-convex *lp*-norm sparse regularization optimization for structural health monitoring. *Eng. Struct.* **2019**, *194*, 346–356. [CrossRef]
12. Tian, L.M.; Wei, J.P.; Hao, J.P. Optimisation of long-span single-layer spatial grid structures to resist progressive collapse. *Eng. Struct.* **2019**, *188*, 394–405. [CrossRef]
13. Park, M.J.; Yoon, S.W.; Kim, Y.C.; Cheon, D.J. Wind pressure characteristics based on the rise–span ratio of spherical domes with openings on the roof. *Buildings* **2022**, *12*, 576. [CrossRef]
14. Ding, M.M.; Luo, B.; Ding, S.Y.; Shen, Y.Z.; Huang, L.F. Experimental investigation and numerical simulation of a levy hinged-beam cable dome. *Buildings* **2021**, *11*, 110. [CrossRef]
15. Yang, Q.S.; Chen, B.; Wu, Y.; Tamura, Y. Wind-induced response and equivalent static wind load of long-span roof structures by combined Ritz-proper orthogonal decomposition method. *J. Struct. Eng.* **2013**, *139*, 997–1008. [CrossRef]
16. Su, N.; Cao, Z.G.; Wu, Y. Fast frequency-domain algorithm for estimating the dynamic wind-induced response of large-span roofs based on Cauchy's residue theorem. *Int. J. Struct. Stab. Dyn.* **2018**, *18*, 1850037. [CrossRef]
17. Wang, Q.H.; Liu, F.H.; Yu, Y. Study on wind-induced response of a large-span roof by using finite particle method. *Structures* **2021**, *34*, 3567–3582. [CrossRef]
18. Li, T.T.; Yan, G.R.; Yuan, F.P.; Chen, G.D. Dynamic structural responses of long-span dome structures induced by tornadoes. *J. Wind Eng. Ind. Aerodyn.* **2019**, *190*, 293–308. [CrossRef]
19. Chen, F.B.; Li, Q.S.; Wu, J.R.; Fu, J.Y. Wind effects on a long-span beam string roof structure: Wind tunnel test, field measurement and numerical analysis. *J. Constr. Steel Res.* **2011**, *67*, 1591–1604. [CrossRef]
20. *GB 50009-2012*; Load Code for the Design of Building Structures. China Architecture and Building Press: Beijing, China, 2012. (In Chinese)
21. He, Y.J.; Zhou, X.H.; Wang, H.S. Wind-induced response analysis of the cylindrical reticulated mega-structures. *Adv. Steel Constr.* **2016**, *12*, 66–82.
22. Zhang, J.S.; Wu, Y.; Shen, S.Z. Wind-induced vibration of single-layer reticulated shell structures. *J. Harbin Institute Technol. (New Series)* **2008**, *15*, 494–498.
23. Zhou, Z.; Li, Z.M.; Meng, S.P.; Wu, J. Wind-induced vibration responses of prestressed double-layered spherical latticed shells. *Int. J. Steel Struct.* **2011**, *11*, 191–202. [CrossRef]
24. Chen, Y.; Liu, G.G.; Sun, B.N. Dynamic response of flat roofs subjected to non-stationary moving microbursts. *Eng. Appl. Comp. Fluid Mech.* **2013**, *7*, 519–532. [CrossRef]
25. Bai, L.J.; Zhang, Y.F. Nonlinear dynamic behavior of steel framed roof structure with self-centering members under extreme transient wind load. *Eng. Struct.* **2013**, *49*, 819–830. [CrossRef]
26. Zhou, Z.; Ding, H.M.; Kong, X.Y. Parametric analysis for a simply supported beam roof structure's wind-induced vibration response under downburst. *J. Vib. Shock* **2017**, *36*, 179–186 + 210. (In Chinese)
27. Chen, L.Z.; Letchford, C.W. A deterministic–stochastic hybrid model of downbursts and its impact on a cantilevered structure. *Eng. Struct.* **2004**, *26*, 619–629. [CrossRef]
28. Chay, M.T.; Albermani, F.; Wilson, R. Numerical and analytical simulation of downburst wind loads. *Eng. Struct.* **2006**, *28*, 240–254. [CrossRef]
29. Wood, G.S.; Kwok, K.C.S.; Motteram, N.A.; Fletcher, D.F. Physical and numerical modelling of thunderstorm downbursts. *J. Wind Eng. Ind. Aerodyn.* **2001**, *89*, 535–552. [CrossRef]
30. Holmes, J.D.; Oliver, S.E. An empirical model of a downburst. *Eng. Struct.* **2000**, *22*, 1167–1172. [CrossRef]
31. Kaimal, J.C.; Wyngaard, J.C.; Izumi, Y.; Cote, O.R. Spectral characteristics of surface-layer turbulence. *Q. J. R. Meteorol. Soc.* **1972**, *98*, 563–589. [CrossRef]
32. Singh, M.P.; Chang, T.S.; Nandan, H. Algorithms for seismic analysis of MDOF systems with fractional derivatives. *Eng. Struct.* **2011**, *33*, 2371–2381. [CrossRef]
33. Li, H.N.; Liu, H.J.; Fu, X.; Zhao, K.; Yang, X.L.; Wen, Z.F. Failure criteria and wind-induced vibration analysis for an offshore platform jacking system. *Int. J. Struct. Stab. Dyn.* **2021**, *21*, 2150105. [CrossRef]
34. *JGJ 7-2010*; Technical Specification for Space Frame Structures. China Architecture and Building Press: Beijing, China, 2010. (In Chinese)
35. Schoen, E.D.; Eendebak, P.T.; Nguyen, M.V.M. Complete enumeration of pure-level and mixed-level orthogonal arrays. *J. Comb. Des.* **2010**, *18*, 123–140. [CrossRef]
36. Keerthana, S.; Pradeep, T.; Gowri Shankar, M.; Prasanna, N. Assessment of constructability and financial aspects of risks in construction industry using design expert. *Int. J. Adv. Sci. Technol.* **2020**, *29*, 4329–4338.